

# Structure and decay pattern of linear-chain state in $^{14}\text{C}$

T. Baba and M. Kimura

*Department of Physics, Hokkaido University, 060-0810 Sapporo, Japan*

(Dated: May 19, 2016)

The linear-chain states of  $^{14}\text{C}$  are theoretically investigated by using the antisymmetrized molecular dynamics. The calculated excitation energies and the  $\alpha$  decay widths of the linear-chain states were compared with the observed data reported by the recent experiments. The properties of the positive-parity linear-chain states reasonably agree with the observation, that convinces us of the linear-chain formation in the positive-parity states. On the other hand, in the negative-parity states, it is found that the linear-chain configuration is fragmented into many states and do not form a single rotational band. As a further evidence of the linear-chain formation, we focus on the  $\alpha$  decay pattern. It is shown that the linear-chain states decay to the excited states of daughter nucleus  $^{10}\text{Be}$  as well as to the ground state, while other cluster states dominantly decay into the ground state. Hence, we regard that this characteristic decay pattern is a strong signature of the linear-chain formation.

## I. INTRODUCTION

A variety of the  $\alpha$  cluster structure are known to exist in light stable nuclei. The most famous example is the Hoyle state (the  $0_2^+$  state of  $^{12}\text{C}$ ) whose dilute gas-like  $3\alpha$  cluster structure has been studied in detail [1–8] and identified well today. The linear-chain configuration of  $3\alpha$  clusters in which  $\alpha$  particles are linearly aligned is an other example of famous and exotic cluster structure. It was firstly suggested by Morinaga [9] to explain the structure of the Hoyle state. However, as mentioned above, it turned out that the Hoyle state does not have the linear-chain configuration but has the dilute gas-like nature. In addition to this, the instability of the linear-chain configuration against the bending motion (deviation from the linear alignment) was pointed out by the antisymmetrized molecular dynamics (AMD) [4] and Fermionic molecular dynamics (FMD) calculations [7]. Thus, the formation of perfectly linear-aligned configuration in  $^{12}\text{C}^*$  looks negative despite of the many years of research.

The interest in the linear-chain configuration is reinforced by the unstable nuclear physics, because the valence neutrons may stabilize it by their glue-like role. Such glue-like role of valence neutron is well known for Be isotopes in which  $2\alpha$  cluster core is assisted by the valence neutrons occupying the molecular-orbits [10–15]. As a natural consequence, we expect that the linear-chain configuration can be realized in neutron-rich C isotopes, and this expectation have been motivating many theoretical and experimental studies [16–28]. Recently, rather promising candidates of linear-chain configuration in  $^{14}\text{C}$  were independently reported by two groups [29, 30]. Both groups observed the  $^4\text{He} + ^{10}\text{Be}$  resonances above the  $\alpha$  threshold energy in both of positive- and negative-parity. The reported energies of the positive-parity resonances measured from the  $\alpha$  threshold are in reasonable agreement with the excitation energies of the linear-chain states predicted by Suhara *et al.* [24] on the basis of the antisymmetrized molecular dynamics (AMD) calculation. Thus, rather promising evidence of the linear-chain

formation has been found.

However, there are still several gaps between theory and experiment which must be resolved to confirm the linear-chain formation in  $^{14}\text{C}$ . First, when measured from the ground state energy, theoretically predicted and experimentally observed excitation energies of the positive-parity resonances disagree. This may be because the effective interaction used in the calculation [31] do not reproduce the  $\alpha$  threshold energy. Second, the experiments report the negative-parity resonances, while the negative-parity linear-chain states were not clearly identified in Ref. [24]. Finally, the experiment [29] reported the  $\alpha$  decay width of the resonances which is a strong evidence of the  $\alpha$  clustering and must be verified by the theoretical calculation. Thus, further theoretical studies are in need to identify the linear-chain states in  $^{14}\text{C}$ .

For this purpose, we investigated the linear-chain states in  $^{14}\text{C}$ . For the sake of the quantitative comparison of the excitation energy, we performed AMD calculation employing Gogny D1S effective interaction [32] which reproduces threshold energies in  $^{14}\text{C}$ . From the AMD wave function, we estimated the  $\alpha$  decay widths of the linear-chain states as well as those of other cluster and non-cluster states. It is found that the calculated excitation energies of the positive-parity linear-chain states are in good agreement with the observation, and only the linear-chain states have large  $\alpha$  decay widths comparable with the observed data. Hence, we consider that the linear-chain formation in the positive-parity state is rather plausible. On the other hand, in the negative-parity state, the linear-chain configuration is fragmented into many states and do not form a single rotational band. As a further evidence of the linear-chain formation, we focus on the  $\alpha$  decay pattern. It is shown that the linear-chain states decay to the excited states of  $^{10}\text{Be}$  as well as the  $^{10}\text{Be}$  ground state, while other cluster states dominantly decay to the  $^{10}\text{Be}$  ground state. This characteristic decay pattern is, if it is observed, a strong signature of the linear-chain formation.

The contents of this paper are as follows. In the next section, the AMD framework and the method to esti-

mate the alpha decay width are briefly outlined. In the III section, the results of the energy variation and generator coordinate method are presented. In the section IV, the energies and  $\alpha$  width of the linear-chain states are compared with the observed data. In the last section, we summarize this study.

## II. THEORETICAL FRAMEWORK

### A. variational calculation and generator coordinate method

The microscopic  $A$ -body Hamiltonian used in this study reads,

$$\hat{H} = \sum_{i=1}^A \hat{t}_i + \sum_{i < j}^A \hat{v}_{ij}^N + \sum_{i < j}^Z \hat{v}_{ij}^C - \hat{t}(c.m.), \quad (1)$$

where the Gogny D1S interaction [32] is used as an effective nucleon-nucleon interaction  $\hat{v}^N$ . It is shown that the Gogny D1S interaction reasonably describes the one neutron-,  $\alpha$ - and  ${}^6\text{He}$ -threshold energies within 1 MeV error. The Coulomb interaction  $\hat{v}^C$  is approximated by a sum of seven Gaussians. The center-of-mass kinetic energy  $\hat{t}(c.m.)$  is exactly removed.

The intrinsic wave function  $\Phi_{int}$  of AMD is represented by a Slater determinant of single particle wave packets,

$$\Phi_{int} = \mathcal{A}\{\varphi_1, \varphi_2, \dots, \varphi_A\} = \frac{1}{\sqrt{A!}} \det[\varphi_i(\mathbf{r}_j)], \quad (2)$$

where  $\varphi_i$  is the single particle wave packet which is a direct product of the deformed Gaussian spatial part [35], spin ( $\chi_i$ ) and isospin ( $\xi_i$ ) parts,

$$\varphi_i(\mathbf{r}) = \phi_i(\mathbf{r}) \otimes \chi_i \otimes \xi_i, \quad (3)$$

$$\phi_i(\mathbf{r}) = \exp\left\{-\sum_{\sigma=x,y,z} \nu_\sigma \left(r_\sigma - \frac{Z_{i\sigma}}{\sqrt{\nu_\sigma}}\right)^2\right\}, \quad (4)$$

$$\chi_i = a_i \chi_\uparrow + b_i \chi_\downarrow, \quad \xi_i = \text{proton or neutron}.$$

The centroids of the Gaussian wave packets  $\mathbf{Z}_i$ , the direction of nucleon spin  $a_i, b_i$ , and the width parameter of the deformed Gaussian  $\nu_\sigma$  are the variational parameters. The intrinsic wave function is projected to the eigenstate of the parity to investigate both of the positive- and negative-parity states,

$$\Phi^\pi = P^\pi \Phi_{int} = \frac{1 + \pi P_x}{2} \Phi_{int}, \quad \pi = \pm, \quad (5)$$

where  $P^\pi$  and  $P_x$  denote parity projector and operator. Using this wave function, the variational energy is defined as

$$E^\pi = \frac{\langle \Phi^\pi | H | \Phi^\pi \rangle}{\langle \Phi^\pi | \Phi^\pi \rangle} \quad (6)$$

By the frictional cooling method [36], the variational parameters are determined so that  $E^\pi$  is minimized. In this study, we add the constraint potential to the variational energy,

$$E'^\pi = \frac{\langle \Phi^\pi | H | \Phi^\pi \rangle}{\langle \Phi^\pi | \Phi^\pi \rangle} + v_\beta (\langle \beta \rangle - \beta_0)^2 + v_\gamma (\langle \gamma \rangle - \gamma_0)^2, \quad (7)$$

where  $\langle \beta \rangle$  and  $\langle \gamma \rangle$  are the quadrupole deformation parameters of the intrinsic wave function defined in Ref. [24, 37], and  $v_\beta$  and  $v_\gamma$  are chosen large enough that  $\langle \beta \rangle$  and  $\langle \gamma \rangle$  are equal to  $\beta$  and  $\gamma$  after the variation. By minimizing  $E'^\pi$ , we obtain the optimized wave function  $\Phi^\pi(\beta, \gamma) = P^\pi \Phi_{int}(\beta, \gamma)$  which has the minimum energy for each set of  $\beta$  and  $\gamma$ .

After the variational calculation, the eigenstate of the total angular momentum  $J$  is projected out from  $\Phi^\pi(\beta, \gamma)$ ,

$$\begin{aligned} \Phi_{MK}^{J^\pi}(\beta, \gamma) &= P_{MK}^J \Phi^\pi(\beta, \gamma) \\ &= \frac{2J+1}{8\pi^2} \int d\Omega D_{MK}^{J*}(\Omega) \hat{R}(\Omega) \Phi^\pi(\beta, \gamma). \end{aligned} \quad (8)$$

Here,  $P_{MK}^J$ ,  $D_{MK}^J(\Omega)$  and  $\hat{R}(\Omega)$  are the angular momentum projector, the Wigner  $D$  function and the rotation operator, respectively. The integrals over Euler angles  $\Omega$  are evaluated numerically.

Then, we perform the GCM calculation by employing the quadrupole deformation parameters  $\beta$  and  $\gamma$  as the generator coordinate. The wave function of GCM reads,

$$\Psi_{Mn}^{J^\pi} = \sum_i \sum_K c_{Kin}^{J^\pi} \Phi_{MK}^{J^\pi}(\beta_i, \gamma_i), \quad (9)$$

where the coefficients  $c_{Kin}^{J^\pi}$  and eigenenergies  $E_n^{J^\pi}$  are obtained by solving the Hill-Wheeler equation [38],

$$\sum_{i'K'} H_{KiK'i'}^{J^\pi} c_{K'i'n}^{J^\pi} = E_n^{J^\pi} \sum_{i'K'} N_{KiK'i'}^{J^\pi} c_{K'i'n}^{J^\pi}, \quad (10)$$

$$H_{KiK'i'}^{J^\pi} = \langle \Phi_{MK}^{J^\pi}(\beta_i, \gamma_i) | \hat{H} | \Phi_{MK'}^{J^\pi}(\beta_{i'}, \gamma_{i'}) \rangle,$$

$$N_{KiK'i'}^{J^\pi} = \langle \Phi_{MK}^{J^\pi}(\beta_i, \gamma_i) | \Phi_{MK'}^{J^\pi}(\beta_{i'}, \gamma_{i'}) \rangle.$$

We also calculate the overlap between  $\Psi_{Mn}^{J^\pi}$  and the basis wave function of the GCM  $\Phi_{MK}^{J^\pi}(\beta_i, \gamma_i)$ ,

$$|\langle \Phi_{MK}^{J^\pi}(\beta, \gamma) | \Psi_{Mn}^{J^\pi} \rangle|^2 / \langle \Phi_{MK}^{J^\pi}(\beta, \gamma) | \Phi_{MK}^{J^\pi}(\beta, \gamma) \rangle, \quad (11)$$

to discuss the dominant configuration in each state described by  $\Psi_{Mn}^{J^\pi}$ .

### B. single particle orbits

Nucleon single-particle energy and orbit are useful to investigate the motion of the valence neutrons around the core nucleus. For this purpose, we construct single-particle Hamiltonian and calculate the neutron single-particle orbits in the intrinsic wave function  $\Phi_{int}(\beta, \gamma)$ .

We first transform the single particle wave packet  $\varphi_i$  to the orthonormalized basis,

$$\tilde{\varphi}_\alpha = \frac{1}{\sqrt{\lambda_\alpha}} \sum_{i=1}^A g_{i\alpha} \varphi_i. \quad (12)$$

Here,  $\lambda_\alpha$  and  $g_{i\alpha}$  are the eigenvalues and eigenvectors of the overlap matrix  $B_{ij} = \langle \varphi_i | \varphi_j \rangle$ . Using this basis, the single particle Hamiltonian is derived,

$$h_{\alpha\beta} = \langle \tilde{\varphi}_\alpha | \hat{t} | \tilde{\varphi}_\beta \rangle + \sum_{\gamma=1}^A \langle \tilde{\varphi}_\alpha \tilde{\varphi}_\gamma | \hat{v}^N + \hat{v}^C | \tilde{\varphi}_\beta \tilde{\varphi}_\gamma - \tilde{\varphi}_\gamma \tilde{\varphi}_\beta \rangle, \\ + \frac{1}{2} \sum_{\gamma, \delta=1}^A \langle \tilde{\varphi}_\gamma \tilde{\varphi}_\delta | \tilde{\varphi}_\alpha^* \tilde{\varphi}_\beta \frac{\delta \hat{v}^N}{\delta \rho} | \tilde{\varphi}_\gamma \tilde{\varphi}_\delta - \tilde{\varphi}_\delta \tilde{\varphi}_\gamma \rangle. \quad (13)$$

The eigenvalues  $\epsilon_s$  and eigenvectors  $f_{\alpha s}$  of  $h_{\alpha\beta}$  give the single particle energies and the single particle orbits,  $\tilde{\phi}_s = \sum_{\alpha=1}^A f_{\alpha s} \tilde{\varphi}_\alpha$ . We also calculate the amount of the positive-parity component in the single-particle orbit,

$$p^+ = |\langle \tilde{\phi}_s | \frac{1 + P_x}{2} | \tilde{\phi}_s \rangle|^2, \quad (14)$$

and angular momenta in the intrinsic frame,

$$j(j+1) = \langle \tilde{\phi}_s | \hat{j}^2 | \tilde{\phi}_s \rangle, \quad |j_z| = \sqrt{\langle \tilde{\phi}_s | \hat{j}_z^2 | \tilde{\phi}_s \rangle}, \quad (15)$$

$$l(l+1) = \langle \tilde{\phi}_s | \hat{l}^2 | \tilde{\phi}_s \rangle, \quad |l_z| = \sqrt{\langle \tilde{\phi}_s | \hat{l}_z^2 | \tilde{\phi}_s \rangle}, \quad (16)$$

which are used to discuss the properties of the single particle orbits.

### C. $\alpha$ reduced width amplitude and decay width

From the GCM wave function, we estimate the  $\alpha$  reduced width amplitude (RWA)  $y_{lj\pi'}(r)$  which is defined as

$$y_{lj\pi'}(r) = \sqrt{\frac{A!}{4!(A-4)!}} \langle \phi_\alpha [ \phi_{\text{Be}}(j^{\pi'}) Y_{l0}(\hat{r}) ] J^\pi M | \Psi_{Mn}^{J^\pi} \rangle, \quad (17)$$

where  $\phi_\alpha$  and  $\phi_{\text{Be}}(j^{\pi'})$  denote the wave functions for  $\alpha$  particle and daughter nucleus  $^{10}\text{Be}$  with spin-parity  $j^{\pi'}$ . The square of the RWA  $|y_{lj\pi'}(r)|^2$  is equal to the probability to observe  $\alpha$  particle and  $^{10}\text{Be}$  with spin-parity  $j^{\pi'}$  at inter-cluster distance  $r$  with relative orbital angular momentum  $l$  in the  $^{14}\text{C}$  described by GCM wave function  $\Psi_{Mn}^{J^\pi}$ .

Using RWA, the partial  $\alpha$  decay widths for the decay process  $^{14}\text{C}(J^\pi) \rightarrow \alpha + ^{10}\text{Be}(j^{\pi'})$  is estimated as

$$\Gamma_{lj\pi'}^\alpha = 2P_l(a) \gamma_{lj\pi'}^2(a), \quad P_l(a) = \frac{ka}{F_l^2(ka) + G_l^2(ka)}, \quad (18)$$

where  $a$  denote the channel radius, and the penetration factor  $P_l$  is given by the Coulomb regular and irregular wave functions  $F_l$  and  $G_l$ . The wave number  $k$  is given by the decay  $Q$ -value and the reduced mass as  $k = \sqrt{2\mu E_Q}$ . The reduced width  $\gamma_{lj\pi'}$  is

$$\gamma_{lj\pi'}^2(a) = \frac{\hbar^2}{2\mu a} [ay_{lj\pi'}(a)]^2. \quad (19)$$

To calculate RWA with reduced computational cost, we employ the method given in Ref. [39] which suggests an approximation validated for sufficiently large inter-cluster distance  $a$ ,

$$|ay_{lj\pi'}(a)|^2 \simeq \sqrt{\frac{\gamma}{2\pi}} |\langle \Phi_{BB}^{J^\pi}(a) | \Psi_{Mn}^{J^\pi} \rangle|^2, \quad (20) \\ \gamma = \frac{4(A-4)}{A} \nu_{BB},$$

which means that RWA is reasonably approximated by the overlap between the GCM wave function and the Brink-Bloch wave function  $\Phi_{BB}^{J^\pi}(a)$  composed of the  $^{10}\text{Be}$  and  $\alpha$  particle with the Gaussian width parameter  $\nu_{BB}$ .

In the case of the present study, since  $^{10}\text{Be}$  is deformed, it must be projected to the eigenstate of the angular momentum. Therefore, we constructed  $\Phi_{BB}^{J^\pi}$  as follows. We first calculate the intrinsic wave function  $\psi_{\text{Be}}$  for  $^{10}\text{Be}$  by the AMD energy variation in which the width parameter  $\nu_{BB}$  is fixed to  $0.16 \text{ fm}^{-2}$ . We obtained two different configurations for  $^{10}\text{Be}$  so-called  $\pi$  and  $\sigma$  configurations. It is known that the former is dominant in the ground band and the latter is dominant in the excited band. Then the  $^{10}\text{Be}$  wave function is projected to the eigenstate of the angular momentum, and combined with the  $\alpha$  cluster wave function to constitute the intrinsic wave function of  $^{14}\text{C}^*$

$$|\Phi_{BB}(a)\rangle = \left| \mathcal{A} \left\{ \psi_\alpha \left( -\frac{10}{14}a \right) \hat{P}_{m0}^j \psi_{\text{Be}} \left( \frac{4}{14}a \right) \right\} \right\rangle, \quad (21)$$

where we assumed that  $\psi_{\text{Be}}$  is parity and axially symmetric, that is validated by the numerical check. Then, the reference wave function is constructed by the angular momentum projection of the total system.

$$\Phi_{BB}^{J^\pi}(a) = \frac{1}{N} \frac{2l+1}{2J+1} \sum_m C_{l0jm}^{Jm} \hat{P}_{Mm}^{J^\pi} |\Phi_{BB}(a)\rangle, \quad (22)$$

Here  $C_{l0jm}^{Jm}$  and  $N$  denotes the Clebsch-Gordan coefficient and the normalization factor. The summation over  $m$  is needed to project the relative angular momentum between  $^{10}\text{Be}$  and  $\alpha$  particle to  $l$ .

## III. RESULTS

### A. Energy surface and intrinsic structures

Figure 1 (a) shows the energy surface as functions of quadrupole deformation parameters  $\beta$  and  $\gamma$  for  $J^\pi = 0^+$

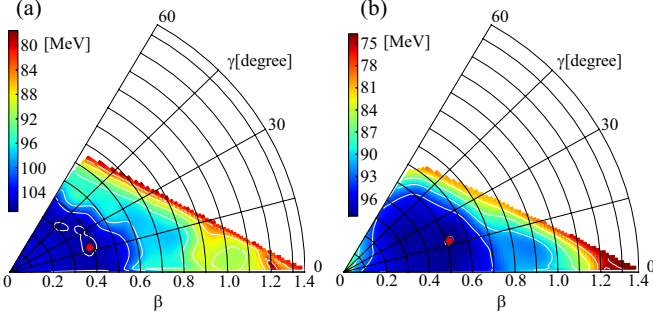


FIG. 1. (color online) The angular momentum projected energy surface for (a) the  $J^\pi = 0^+$  state and (b)  $J^\pi = 1^-$  state as functions of quadrupole deformation parameters  $\beta$  and  $\gamma$ . The circles show the position of the energy minima.

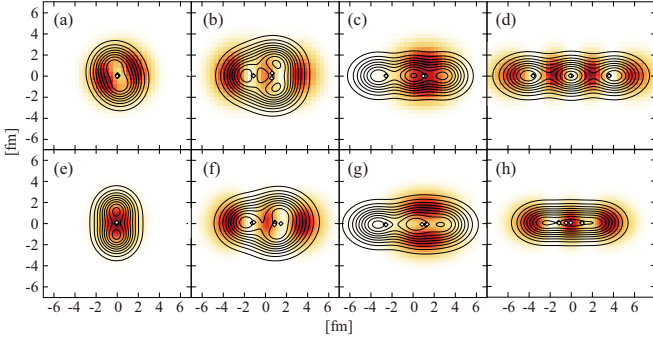


FIG. 2. (color online) The density distribution of (a)-(d) the positive states and (e)-(h) negative parity states. The contour lines show the proton density distributions. The color plots show the single particle orbits occupied by the most weakly bound neutron. Open boxes show the centroids of the Gaussian wave packets describing protons.

states obtained by the constraint variational calculation and angular momentum projection. The circles on the energy surfaces show the position of the energy minima.

The energy minimum of the  $0^+$  state is located at  $(\beta, \gamma) = (0.36, 14^\circ)$  with the binding energy of 106.1 MeV. It is interesting that this minimum state is deformed, as seen in its intrinsic density distribution shown in Fig. 2 (a), despite of the neutron magic number  $N = 8$ . However, the deformation is not large enough to break the neutron magicity as the last valence neutron occupies  $p$ -wave that can be deduced from the density distribution of the valence neutron orbit shown in Fig. 2 (a).

In the oblate deformed region, the different structure which we call triangular configuration appears. Fig. 2 (b) shows the density distribution of the wave function located at  $(\beta, \gamma) = (0.60, 25^\circ)$ . The proton density distribution have triangular shape showing possible formation of  $3\alpha$  cluster core with triangle configuration. Indeed, as mentioned later, the excited states composed of this configuration have larger  $\alpha$  reduced widths than the ground state. Owing to the parity asymmetric shape, the valence proton orbit is an admixture of the positive- and

TABLE I. The properties of the most weakly bound proton and neutron orbits in the configurations shown in Fig. 2 (a)-(h). The column occ. shows the number of the nucleon occupying the orbit. When two valence nucleons occupy the almost degenerated orbits, the single-particle properties are averaged and occ. is equal to 2. Other columns show the single particle energy  $\varepsilon$  in MeV, the amount of the positive-parity component  $p^+$  and the angular momenta defined by Eqs. (14)-(16).

		occ.	$\varepsilon$	$p^+$	$j$	$ j_z $	$l$	$ l_z $
(a)	proton	2	-17.4	0.00	1.5	1.5	1.1	1.0
	neutron	2	-6.6	0.22	1.1	0.6	1.2	0.9
(b)	proton	2	-14.1	0.08	1.6	1.5	1.2	1.0
	neutron	2	-5.3	0.98	2.2	0.5	1.8	0.3
(c)	proton	2	-12.5	0.97	2.2	0.5	2.0	0.2
	neutron	2	-7.0	0.09	1.8	1.5	1.4	1.0
(d)	proton	2	-15.6	0.99	2.5	0.5	2.3	0.1
	neutron	2	-4.4	0.01	2.8	0.5	2.6	0.1
(e)	proton	2	-16.0	0.00	1.5	1.4	1.1	1.0
	neutron	1	-3.8	0.99	2.2	0.5	1.8	0.4
(f)	proton	1	-12.6	0.53	1.9	0.9	1.6	0.8
	neutron	2	-6.6	0.98	2.1	0.6	1.8	0.3
(g)	proton	1	-12.4	0.72	2.3	0.9	2.1	0.6
	neutron	2	-7.2	0.11	1.9	1.4	1.6	1.0
(h)	proton	1	-13.1	0.52	1.9	1.0	1.6	0.8
	neutron	2	-8.2	0.92	2.2	0.7	1.9	0.4

negative-parity component as confirmed from the properties of the single-particle orbit listed in Table I. The table also shows that two valence neutrons occupy positive-parity orbit ( $sd$ -shell) indicating the  $2\hbar\omega$  excitation. It is noted that a similar configuration, *i.e.* a triangular  $3\alpha$  cluster core with  $2\hbar\omega$  excited valence neutrons, was also found in  $^{16}\text{C}$  [27].

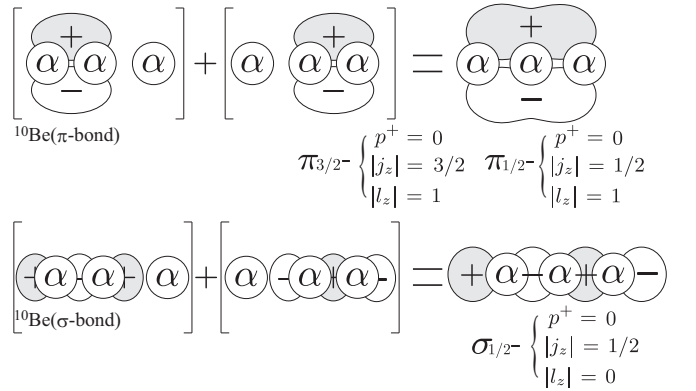


FIG. 3. The schematic figure showing the  $\pi$  and  $\sigma$ -orbits around the linear chain. The combination of the  $p$  orbits perpendicular to the symmetry axis generates  $\pi$  orbits, while the combination of parallel orbits generates  $\sigma$  orbit.

In the strongly deformed region, the linear-chain configurations appear. There is an energy plateau around the local energy minimum at  $(\beta, \gamma) = (1.00, 0)$  which approximately corresponds to the deformation ratio equal to 3 : 1. As clearly seen in its density distribution shown in Fig. 2 (c), this local energy minimum has pronounced  $3\alpha$  cluster structure with linear alignment. The properties of the proton single-particle orbit shows that the last two protons are promoted into  $sd$ -shell, that is because of the Pauli principle in the linear-chain configuration. The density distribution and properties of the valence neutron orbits show that they correspond to the  $\pi$ -orbit of the molecular-orbit picture which is schematically illustrated in Fig. 3. Namely, the valence neutron orbit is a linear combination of the  $p$ -orbits perpendicular to the symmetry axis and has the angular momenta  $|j_z| = 1.5$  and  $|l_z| = 1.0$ . We call this configuration  $\pi$ -bond linear chain in the following. This property of the valence neutron orbit is common to that found in  $^{16}\text{C}$  [27]. However, it should be noted that the  $\pi$ -orbit of  $^{14}\text{C}$  do not have parity symmetric distribution but is localized between the center and right  $\alpha$  clusters. In other words, this configuration is the parity asymmetric and has  $^4\text{He}+^{10}\text{Be}$ -like structure, which is consistent with the discussion made in Ref. [24, 33]. Because this linear-chain configuration and the triangular configuration explained above have asymmetric internal structures, we expect that the corresponding negative-parity partners may exist and constitute the inversion doublets.

With further increase of the deformation, the other linear-chain configuration which we call  $\sigma$ -bond linear chain appears around  $(\beta, \gamma) = (1.27, 0)$  which was not mentioned in Ref. [24]. From the density distribution (Fig. 2 (d)), it is clear that this configuration has another valence neutron orbit that correspond to the  $\sigma$ -orbit which is a linear combination of  $p$ -orbit parallel to the symmetry axis and has the angular momenta  $|j_z| \approx 0.50$  and  $|l_z| \approx 0$ . It is interesting to note that this configuration has parity symmetric shape, and hence, do not have its negative-parity partner.

The energy minimum of the energy surface for the  $1^-$  states (Fig. 1 (b)) is located at  $(\beta, \gamma) = (0.52, 19^\circ)$  with the binding energy of  $-98.2$  MeV, and its density distribution is described in Fig. 2(e). From Tab. I, we see that this minimum has the same proton configuration with the positive-parity minimum, but a neutron is excited into  $sd$ -shell from  $p$ -shell ( $1p1h$  configuration).

Because the triangular configuration and the  $\pi$ -bond linear-chain of the positive parity are parity asymmetric, their counterparts appear in the negative-parity states. Fig. 2 (f) and (g) show the triangular configuration and the  $\pi$ -bond linear-chain configuration in the negative-parity state located at  $(\beta, \gamma) = (0.72, 14^\circ)$  and  $(1.05, 3^\circ)$ , respectively. Although the cluster cores are more distorted than the positive-parity states, their neutron single-particle configurations are similar to their positive-parity counterparts. However, as explained in the next section, these cluster configurations do not form single

rotational band and are fragmented into many states because of the mixing with other non-cluster states. For example, the negative-parity  $\pi$ -bond linear-chain strongly mixes with the strongly deformed non-cluster states such as the configuration shown in Fig. 2 (h), that makes it impossible to identify the linear-chain rotational state uniquely.

## B. Excitation spectrum

Figure 4 shows the spectrum of the positive-parity states obtained by the GCM calculation. The properties of the several selected states are listed in Tab. II. We classified the excited states which have large  $\alpha$  reduced widths as cluster states. The detail of the  $\alpha$  reduced widths is given in the section IV B. In the case of the positive-parity states, the cluster states are assigned in the rotational bands without uncertainty, because the band member states are connected by the strong  $E2$  transitions as listed in Tab. III.

TABLE II. Excitation energies (MeV) and proton and neutron root-mean-square radii (fm) of several selected states. Numbers in the parenthesis are the observed data [40, 41].

band	$J^\pi$	$E_x$	$r_p$	$r_n$
ground	$0_1^+$	0.00	2.53	2.58
	$2_1^+$	8.41 (7.01)	2.58 (2.34)	2.69
triangular $K^\pi = 0^+$	$0_2^+$	7.49	2.67	2.92
	$2_2^+$	9.26	2.64	2.83
	$4_1^+$	12.00	2.65	2.89
triangular $K^\pi = 2^+$	$2_3^+$	10.99	2.68	2.92
	$3_1^+$	12.03	2.68	2.92
	$4_2^+$	13.83	2.68	2.92
$\pi$ -bond linear chain	$0_4^+$	14.64	3.27	3.20
	$2_5^+$	15.73	3.37	3.28
	$4_5^+$	17.98	3.33	3.24
	$6_2^+$	21.80	3.39	3.30
$\sigma$ -bond linear chain	$0_7^+$	22.16	3.91	4.12
	$2_{10}^+$	22.93	4.02	4.21
	$4_{11}^+$	24.30	3.97	4.15

The ground state and the first excited state ( $2_1^+$ ) are dominantly composed of the configurations around the energy minimum of the energy surface. The ground state has the largest overlap with the configuration shown in Fig. 2 (a) that amounts to 0.98, and the calculated binding energy is  $-106.3$  MeV that is reasonably close to the observed value of  $-105.3$  MeV. The excitation energy of the  $2_1^+$  state is also reasonably described.

Owing to its triaxial deformed shape, the triangular configuration generates the rotational bands built on the

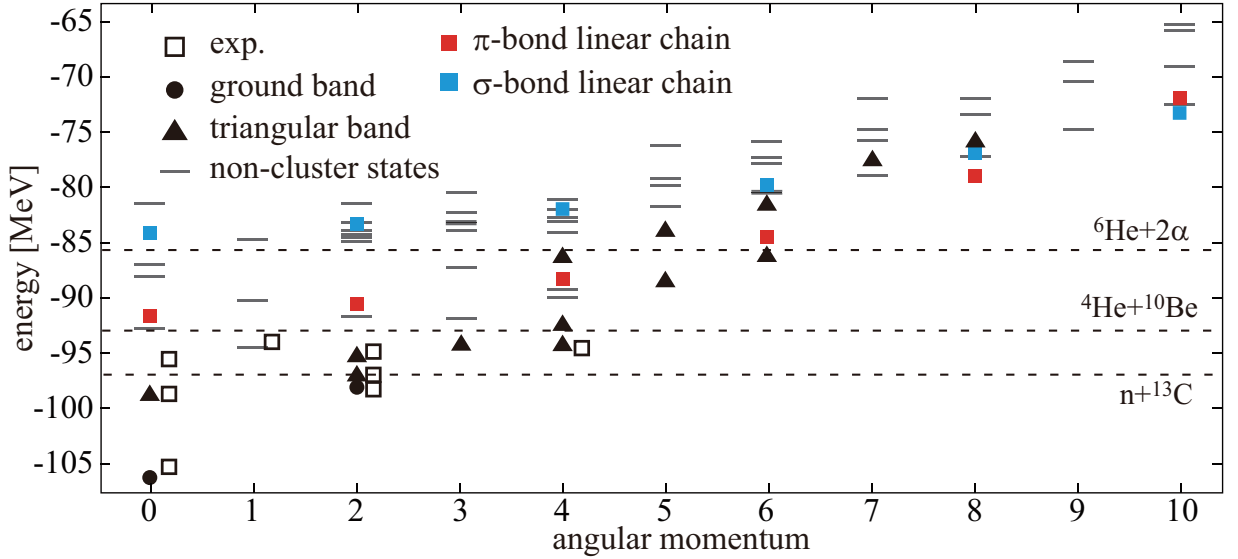


FIG. 4. (color online) The positive-parity energy levels up to  $J^\pi = 10^+$ . Open boxes show the observed states with the definite spin-parity assignments taken from Ref. [40], and other symbols show the calculated result. The filled circles, triangles and filled boxes show the ground, triangular and linear-chain bands, while lines show the non-cluster states.

TABLE III. The calculated in-band  $B(E2)$  strengths for the low-spin positive-parity states in unit of  $e^2\text{fm}^4$ . For the negative-parity states, the transitions between the low-spin fragmented cluster states (diamonds in Fig. 5) are shown and the transitions less than  $10 e^2\text{fm}^4$  are not shown. The number in parenthesis is the observed data [42].

	$J_i \rightarrow J_f$	$B(E2; J_i \rightarrow J_f)$
ground $\rightarrow$ ground	$2_1^+ \rightarrow 0_1^+$	8.1 (3.74)
triangular $K^\pi = 0^+$	$2_2^+ \rightarrow 0_2^+$	7.6
$\rightarrow$ triangular $K^\pi = 0^+$	$4_1^+ \rightarrow 2_2^+$	7.9
	$6_1^+ \rightarrow 4_2^+$	19.8
triangular $K^\pi = 2^+$	$3_1^+ \rightarrow 2_3^+$	17.6
$\rightarrow$ triangular $K^\pi = 2^+$	$4_2^+ \rightarrow 3_1^+$	8.5
	$4_2^+ \rightarrow 2_3^+$	5.4
$\pi$ -bond linear chain	$2_5^+ \rightarrow 0_4^+$	165.5
$\rightarrow \pi$ -bond linear chain	$4_5^+ \rightarrow 2_5^+$	257.4
	$6_2^+ \rightarrow 4_5^+$	276.5
$\sigma$ -bond linear chain	$2_{10}^+ \rightarrow 0_7^+$	441.9
$\rightarrow \sigma$ -bond linear chain	$4_{11}^+ \rightarrow 2_{10}^+$	655.9
negative parity states	$3_4^- \rightarrow 1_3^-$	21.9
	$3_5^- \rightarrow 1_3^-$	32.4
	$3_6^- \rightarrow 1_5^-$	60.1
	$3_{10}^- \rightarrow 1_5^-$	31.5
	$5_2^- \rightarrow 3_4^-$	63.0
	$5_4^- \rightarrow 3_5^-$	54.5
	$5_7^- \rightarrow 3_6^-$	53.9

$0_2^+$  and  $2_3^+$  states that are shown by triangles in Fig. 4.

We call them  $K^\pi = 0^+$  and  $2^+$  bands, respectively in the following, although the mixing of the  $K$  quantum number in their GCM wave functions is not negligible. Compared to the linear-chain states, these bands have less pronounced clustering and  $\alpha$  clusters are considerably distorted, therefore the band head energies are well below the cluster thresholds. The member states have large overlap with the configuration shown in Fig. 2 (b) which amount to, for example, 0.91 in the case of the  $0_2^+$  state.

The linear-chain configurations generate two rotational bands in Fig. 4. The first one which we call  $\pi$ -bond linear-chain band is built on the  $0_4^+$  state at 14.6 MeV close to the  $\alpha$  threshold energy and composed of the  $\pi$ -bond linear-chain configurations. The band head state (the  $0_4^+$  state) has large overlap with the configuration shown in Fig.2 (c) which amounts to 0.87. The other band which we call  $\sigma$ -bond linear-chain band is built on the  $0_7^+$  state at 22.2 MeV (about 9.18 MeV above the  $\alpha$  threshold) and composed of the  $\sigma$ -bond linear-chain configurations shown in Fig.2 (d). This intrinsic wave function has the largest overlap with the band head state that amounts to 0.99. The  $\pi$ -bond linear-chain band is the candidate of the observed resonances and the comparison with the observation is discussed in the next section.

In the case of the negative-parity states shown in Fig. 5, it is found that the  $\alpha$  cluster configurations are fragmented into many excited states. As a result, the  $E2$  transition strengths are also spread to several states, and it makes the band assignment ambiguous. For example, as listed in Tab. III, there are two  $3^-$  states that strongly decay to the  $1_3^-$  state. Those fragments of the cluster configurations are shown by diamond symbols which are mainly composed of the configurations shown in Fig.

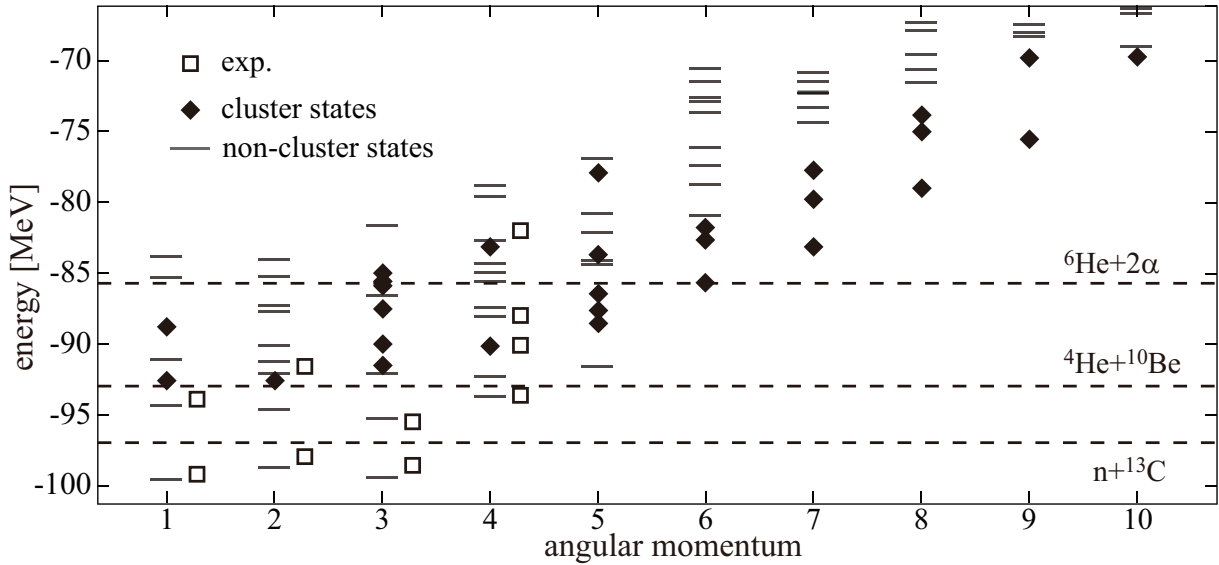


FIG. 5. The negative-parity energy levels up to  $J^\pi = 10^-$ . Open boxes show the observed states with the definite spin-parity assignments taken from Ref. [40], and other symbols show the calculated result. The diamonds show the cluster states having non-negligible  $\alpha$  reduced widths, while lines show the non-cluster states.

2(f), (g), (h) and other non-cluster configurations. For example, the  $1_3^-$  state has the largest overlap with the configuration shown in Fig. 2 (h) that amounts to 0.93. But, at the same time, this state also have large overlap with the triangular configuration shown in Fig. 2 (f) and the  $\pi$ -bond linear-chain shown in Fig. 2 (g) which amounts to 0.85 and 0.70, respectively. This means that these fragmented states are the mixture of cluster states and non-cluster states. The fragmentation of the cluster configurations can be more clearly seen in their  $\alpha$  reduced widths which are discussed in the next section.

#### IV. DISCUSSION

##### A. Excitation energies of the linear-chain bands

In this section, we focus on the excitation energies of the linear-chain bands and compare them with the experiments [20, 29, 30]. The results of the present calculation and the experimental candidates are summarized in Fig. 6. By the measurement of the  ${}^9\text{Be}({}^7\text{Li}, d){}^{14}\text{C}$  reaction, von Oertzen *et al.* [20] reported a candidate of the linear-chain band whose band-head energy is below the  $\alpha$  threshold energy. Freer *et al.* [29] and Fritsch *et al.* [30] independently measured  ${}^4\text{He} + {}^{10}\text{Be}$  resonant scattering using radioactive  ${}^{10}\text{Be}$  beam, and reported the candidates above the threshold energy. The resonance energies of  $4^+$  state reported by Freer *et al.* and Fritsch *et al.* are close to each other, but those of  $2^+$  state differ. However, it must be kept in mind that the assignment of the  $2^+$  state by Freer *et al.* is tentative as mentioned in their report.

Then, we see that the calculated energy of the  $\pi$ -bond linear chain is close to the resonances observed in

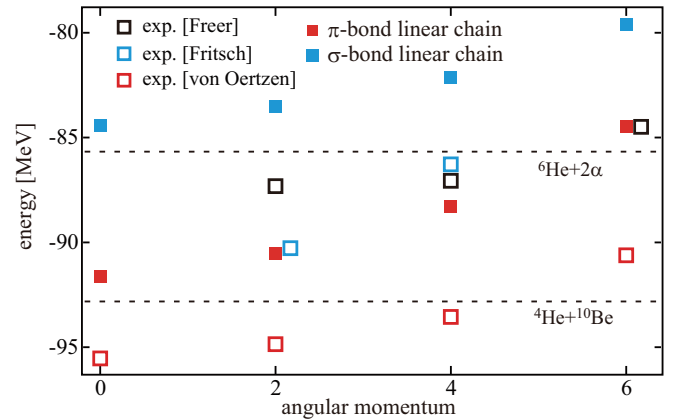


FIG. 6. (color online) The calculated and observed linear-chain candidates in positive parity. Open boxes show the observed data reported by Refs. [20, 29, 30]. Filled boxes show the energies of the  $\pi$ -bond and  $\sigma$ -bond linear chain states.

the  ${}^4\text{He} + {}^{10}\text{Be}$  resonant scattering except for the tentatively assigned  $2^+$  state. In addition, as discussed in the next section, the  $\alpha$  reduced widths of the  $\pi$ -bond linear chain and those observed resonances are close to each other. Hence, we conclude that the resonances observed in the  ${}^4\text{He} + {}^{10}\text{Be}$  resonant scattering should be the  $\pi$ -bond linear chain. The excited states reported by von Oertzen *et al.* are approximately 5 MeV lower than the  $\pi$ -bond linear chain, and it energetically corresponds to the triangular band. The measurement of the  $\alpha$  widths of those candidate will make this assignment sure. The  $\sigma$ -bond linear chain is energetically located higher than any observed resonances and does not have the experi-



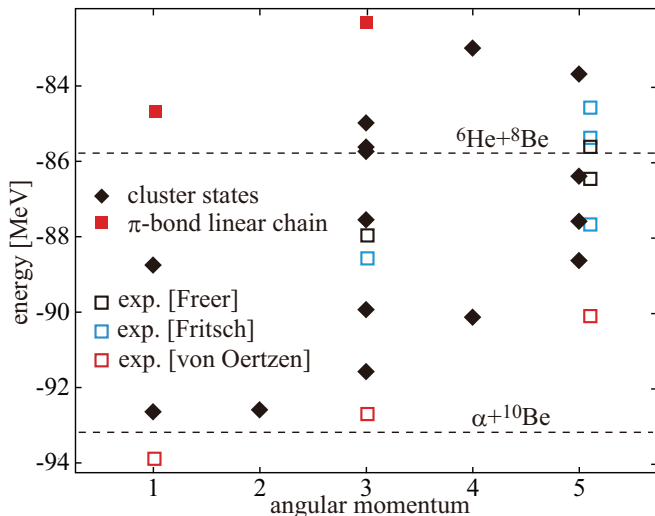


FIG. 7. (color online) The calculated cluster states and observed linear-chain candidates in negative parity. Open boxes show the observed data reported by Refs. [20, 29, 30]. Filled diamonds are the fragmented excited states with cluster configuration. Red boxes shows the  $\pi$ -bond linear-chain projected to negative-parity.

mental counterpart. As we see later, the  $\sigma$ -bond linear chain is dominantly composed of the  ${}^4\text{He} + {}^{10}\text{Be}(0_2^+)$  and  ${}^4\text{He} + {}^{10}\text{Be}(2_2^+)$  component. Therefore, we consider that it is not easy to populate this band by ordinary transfer reaction or resonant scattering.

Fig. 7 summarizes the negative-parity results. In contrast to the positive parity, there are so many fragments of the cluster configurations in the theoretical result. As a result, the correspondence between the theory and experiment is not unique. We also performed an additional test calculation. We pickup the  $\pi$ -bond linear-chain configuration with positive parity shown in Fig. 2 (c) and artificially project it to the negative-parity to estimate the energy of the ideal  $\pi$ -bond linear chain with negative-parity. The results is shown by the red filled boxes in Fig. 7. We see that the energy of the ideal linear-chain is too high to be assigned to the observed resonances. Thus, the present calculation does not support the formation of the linear chain in negative parity.

## B. Reduced width

Figure 8 shows the  $\alpha$  reduced widths of several selected low-spin states with positive parity. The decay channels are indicated as  $[{}^{10}\text{Be}(j^\pi) \otimes l]$  where  $j^\pi$  and  $l$  denote the angular momenta of the  ${}^{10}\text{Be}$  ground band and the relative motion between  ${}^{10}\text{Be}$  and  $\alpha$  particle, respectively. Here,  ${}^{10}\text{Be}$  is assumed to have two neutrons in  $\pi$ -orbit. The dominance of the  $\pi$ -bond configuration in the  ${}^{10}\text{Be}$  was confirmed by the observations [43].

There are two prominent features to be noted in these results. The first is the magnitude of the reduced widths.

The  $\pi$ -bond linear-chain band (the  $0_4^+$ ,  $2_5^+$ ,  $4_5^+$  and  $6_2^+$  states) have large reduced widths compared to the triangular bands and the ground state. It is also noted that the  $\alpha$  reduced widths of other excited states are also smaller than the  $\pi$ -bond linear-chain band, and even smaller than or comparable with the triangular bands. Hence, in the calculated energy region, the  $\pi$ -bond linear chain band has the largest reduced width. In Fig. 8(b)-(d), the observed reduced widths of the linear-chain candidates [29] are also shown for  $2^+$ ,  $4^+$  and  $6^+$  states. Since the decay to the  ${}^{10}\text{Be}$  ground state was *assumed* in the R-matrix analysis made in Ref. [29], those values may be compared with the calculated results for the  $[{}^{10}\text{Be}(0_1^+) \otimes l]$  channel, and we see that only the  $\pi$ -bond linear-chain band can explain the magnitude of the observed reduced widths. Thus, both of the observed excitation energies and reduced widths are reasonably explained by the  $\pi$ -bond linear-chain band, and we consider that the linear-chain formation in the positive-parity looks plausible.

It is also interesting to note that the other linear-chain band, *i.e.* the  $\sigma$ -bond linear-chain band, has suppressed reduced widths despite of their prominent  $\alpha$  clustering. The reason is simple. Because the  $\sigma$ -bond linear-chain band does not have valence neutron in  $\pi$ -orbit, it is orthogonal to the decay channels to the  ${}^{10}\text{Be}$  ground state that has  $\pi$ -orbit neutron. This is confirmed in Fig. 8 (e) where the reduced widths for the decays to the  ${}^{10}\text{Be}$  with  $\sigma$ -bond (the excited rotational band of  ${}^{10}\text{Be}$ ) are shown. Since other bands do not have valence neutrons in  $\sigma$ -orbit, their reduced widths are suppressed, and only the  $\sigma$ -bond linear-chain band has large widths.

Another point to be noted is the decay pattern of the  $\pi$ -bond linear-chain band. The reduced widths in the  $[{}^{10}\text{Be}(2_1^+) \otimes l]$  channels are as large as or even larger than those in the  $[{}^{10}\text{Be}(0_1^+) \otimes l]$  channel. This dominance of the  ${}^{10}\text{Be}(2_1^+)$  component in the  $\pi$ -bond linear-chain band is owe to its unique structure. When three  $\alpha$  particles are linearly aligned, because of the strong angular correlation between  $\alpha$  particles, the  ${}^{10}\text{Be}(2_1^+)$  and  ${}^{10}\text{Be}(4_1^+)$  components become large. This property is in contrast to the Hoyle state where  $\alpha$  particles are mutually orbiting with  $l = 0$ , and hence, the  ${}^8\text{Be}(0_1^+)$  component dominates [8]. Similar property of the linear-chain configuration were also discussed in  ${}^{12}\text{C}$ [34]. Therefore, if the large contamination of the  ${}^{10}\text{Be}(2_1^+)$  component is confirmed, it will be a strong evidence for the linear-chain formation.

The  ${}^{10}\text{Be}(2_1^+)$  component in the triangular bands also show an interesting feature. There are two triangular bands with  $K^\pi = 0^+$  and  $K^\pi = 2^+$ . The  $0_2^+$ ,  $2_2^+$  and  $4_1^+$  states are the member of the  $K^\pi = 0^+$  band, while the  $2_3^+$ ,  $4_2^+$  and  $6_1^+$  are member of the  $K^\pi = 2^+$  band. Here, we clearly see that the  ${}^{10}\text{Be}(0_1^+)$  component is dominant in the  $K^\pi = 0^+$  band, while the  ${}^{10}\text{Be}(2_1^+)$  component is dominant in the  $K^\pi = 2^+$  band. This feature is explained by Fig. 9. In the triangular bands,  ${}^4\text{He}$  and  ${}^{10}\text{Be}$  are placed in a triangular shape and the intrinsic  $z$ -axis is chosen to be perpendicular to the deformation axis of



$^{10}\text{Be}$ . Since the  $K$  quantum number is the angular momentum directed to the intrinsic  $z$ -axis,  $K$  must be equal to the angular momentum of  $^{10}\text{Be}$ . This makes the difference in the amount of the  $^{10}\text{Be}(2_1^+)$  component in the  $K^\pi = 0^+$  and  $2^+$  bands.

For the negative parity, we show the states which have the reduced widths larger than  $0.1 \text{ MeV}^{1/2}$  in Fig. 8 (f)-(h). We can see that there are many states which have non-negligible  $\alpha$  reduced widths, and not able to identify the linear-chain band. As already mentioned, the linear-chain configurations are coupled with the non-cluster configurations and fragmented into many states as found in Ref. [24]. We also see that none of the calculated state can explain the observed reduced widths that are twice larger than the present results. This requires further theoretical study of the negative-parity states, although the current result looks negative to the linear-chain formation in the negative-parity.

## V. SUMMARY

In order to investigate the existence of the linear-chain state, we have studied the excited states of  $^{14}\text{C}$  based on the AMD calculations.

In the positive-parity states, we found that three different configurations appear depending on the magnitude of the deformation and the valence neutron configurations. At oblate deformed region, the triangular configuration of  $3\alpha$  cluster was obtained, while at strong deformed prolate region, two different linear-chain configurations with valence neutrons in  $\pi$ -orbit and  $\sigma$ -orbit were obtained.

These cluster configurations generate clear rotational bands. The  $\pi$ -bond linear chain generates a rotational band around the  $\alpha$  threshold energy, while triangular and  $\sigma$ -bond linear chain generate rotational bands well

below and well above the threshold. The energy of the  $\pi$ -bond linear chain is in reasonable agreement with the resonances observed by the  $^4\text{He} + ^{10}\text{Be}$ , while the triangular band is close to the excited states observed by the  $^9\text{Be}(^7\text{Li},d)^{14}\text{C}$  reaction. The analysis of the  $\alpha$  reduced width confirms the assignment of the  $\pi$ -bond linear chain to the observed resonances, because the calculated and measured widths showed reasonable agreement. Thus, the positive-parity linear-chain formation in  $^{14}\text{C}$  looks plausible. Furthermore, the calculation predicts that the  $\pi$ -bond linear-chain will also decay to the  $^{10}\text{Be}(2_1^+)$  as well as to the  $^{10}\text{Be}(0_1^+)$ . This characteristic decay pattern will be, if measured, another evidence of the linear-chain formation.

In the negative-parity states, the negative-parity partners of the cluster states were also obtained by the energy variation. However, because of the mixing with the non-cluster configurations, these cluster configurations are fragmented into many excited states. As a result, many excited states that have sizable  $\alpha$  reduced width are obtained, and it makes the correspondence between the theory and experiment ambiguous. Thus, the present result is negative for the linear-chain formation in the negative-parity, although further studies are in need to identify the structure of the observed negative-parity resonances.

## ACKNOWLEDGMENTS

The authors acknowledges the fruitful discussions with Dr. Suhara, Dr. Kanada-En'yo, Dr. Fritsch, Mr. Koyama and Dr. H. Otsu. One of the authors (M.K.) acknowledges the support by the Grants-in-Aid for Scientific Research on Innovative Areas from MEXT (Grant No. 2404:24105008) and JSPS KAKENHI Grant No. 16K05339.

- 
- [1] E. Uegaki, S. Okabe, Y. Abe and H. Tanaka, *Progr. Theor. Phys.* **57**, 1262 (1977); *ibid.* **62**, 1621 (1979).
  - [2] M. Kamimura, *Nucl. Phys. A* **351**, 456 (1981).
  - [3] P. Descouvemont and D. Baye, *Phys. Rev. C* **36**, 54 (1987).
  - [4] Y. Kanada-En'yo *Phys. Rev. Lett.* **81** 5291 (1998).
  - [5] A. Tohsaki, H. Horiuchi, P. Schuck, G. Röpke, *Phys. Rev. Lett.* **87**, 192501 (2001).
  - [6] Y. Funaki, A. Tohsaki, H. Horiuchi, P. Schuck, G. Röpke, *Phys. Rev. C* **67**, 051306 (2003).
  - [7] M. Chernykh, H. Feldmeier, T. Neff, P. von Neumann-Cosel and A. Richter, *Phys. Rev. Lett.* **98**, 032501 (2007).
  - [8] Y. Funaki, H. Horiuchi, and A. Tohsaki, *Prog. Part. Nucl. Phys.* **82** 78-132 (2015).
  - [9] H. Morinaga, *Phys. Rev.* **101**, 254 (1956).
  - [10] M. Seya, M. Kohno and S. Nagata, *Prog. Theor. Phys.* **65**, 204 (1981).
  - [11] W. von Oertzen, *Z. Phys. A* **354**, 37 (1996); *ibid.* **357**, 355 (1997).
  - [12] N. Itagaki and S. Okabe, *Phys. Rev. C* **61**, 044306 (2000).
  - [13] Y. Kanada-En'yo, H. Horiuchi and A. Doté, *Phys. Rev. C* **60**, 064304 (1999).
  - [14] Y. Kanada-En'yo, M. Kimura and H. Horiuchi, *C. R. Physique* **4**, (2003) 497.
  - [15] Y. Kanada-En'yo, M. Kimura and A. Ono, *PTEP* **2012**, (2012) 01A202.
  - [16] N. Itagaki, S. Okabe, K. Ikeda and I. Tanihata, *Phys. Rev. C* **64** (2001) 014301.
  - [17] B. J. Greenhalgh, *et al.*, *Phys. Rev. C* **66** (2002) 027302.
  - [18] W. von Oertzen and H. G. Böhlen, *C. R. Physique* **4**, 465 (2003).
  - [19] H. G. Böhlen, *et al.*, *Phys. Rev. C* **68** (2003) 054606.
  - [20] W. von Oertzen, *et al.*, *Eur. Phys. J. A* **21** (2004) 193.
  - [21] N. I. Ashwood, *et al.*, *Phys. Rev. C* **70**, 064607 (2004).
  - [22] N. Itagaki, W. von Oertzen and S. Okabe, *Phys. Rev. C* **74** (2006) 067304.
  - [23] D. L. Price *et al.*, *Phys. Rev. C* **75** (2007) 014305.

- [24] T. Suhara and Y. Kanada-En'yo, Phys. Rev. C **82** (2010) 044301.
- [25] J. Maruhn, N. Loebl, N. Itagaki, M. Kimura, Nucl. Phys. A **883**, 1 (2010).
- [26] N. Furutachi and M. Kimura, Phys. Rev. C **83** (2011) 021303(R).
- [27] T. Baba, Y. Chiba and M. Kimura, Phys. Rev. C **90**, 064319 (2014)
- [28] P. W. Zhao, N. Itagaki, and J. Meng, Phys. Lett. **115**, 022501 (2015).
- [29] M. Freer, *et al.*, Phys. Rev. C **90**, 054324 (2014).
- [30] A. Fritsch *et al.*, Phys. Rev. C **93**, 014321 (2016).
- [31] A. Volkov, Nucl. Phys. **74**, 33 (1965).
- [32] J. F. Berger, M. Girod, and D. Gogny, Comput. Phys. Comm. **63** (1991) 365.
- [33] T. Suhara and Y. Kanada-En'yo, Phys. Rev. C **84**, 024328 (2011).
- [34] Y. Suzuki, H. Horiuchi, and K. Ikeda, Prog. Theor. Phys. **47**, 5 (1972).
- [35] M. Kimura, Phys. Rev. C **69** (2004) 044319.
- [36] Y. Kanada-En'yo and H. Horiuchi, Prog. Theor. Phys. **93**, 115 (1995).
- [37] M. Kimura, R. Yoshida and M. Isaka, Prog. Theor. Phys. **127**, 287 (2012).
- [38] D. L. Hill and J. A. Wheeler, Phys. Rev. **89**, 1102 (1953).
- [39] Y. Kanada-En'yo, T. Suhara, and Y. Taniguchi, Prog. Theor. Exp. Phys. **2014**, 073D02.
- [40] F. Ajzenberg-Selove, Nucl. Phys. A **523**, 1 (1991).
- [41] I. Angelia and K. P. Marinovab, At. Data Nucl. Data Tables **99**, 69 (2013).
- [42] S. Raman, C. W. Nestor Jr., and P. Tikkanen, At. Data Nucl. Data Tables **78**, 1 (2001).
- [43] D. L. Powell, G. M. Crawley, B. V. N. Rao and B. A. Robson, Nucl. Phys. A **147**, 65 (1970).

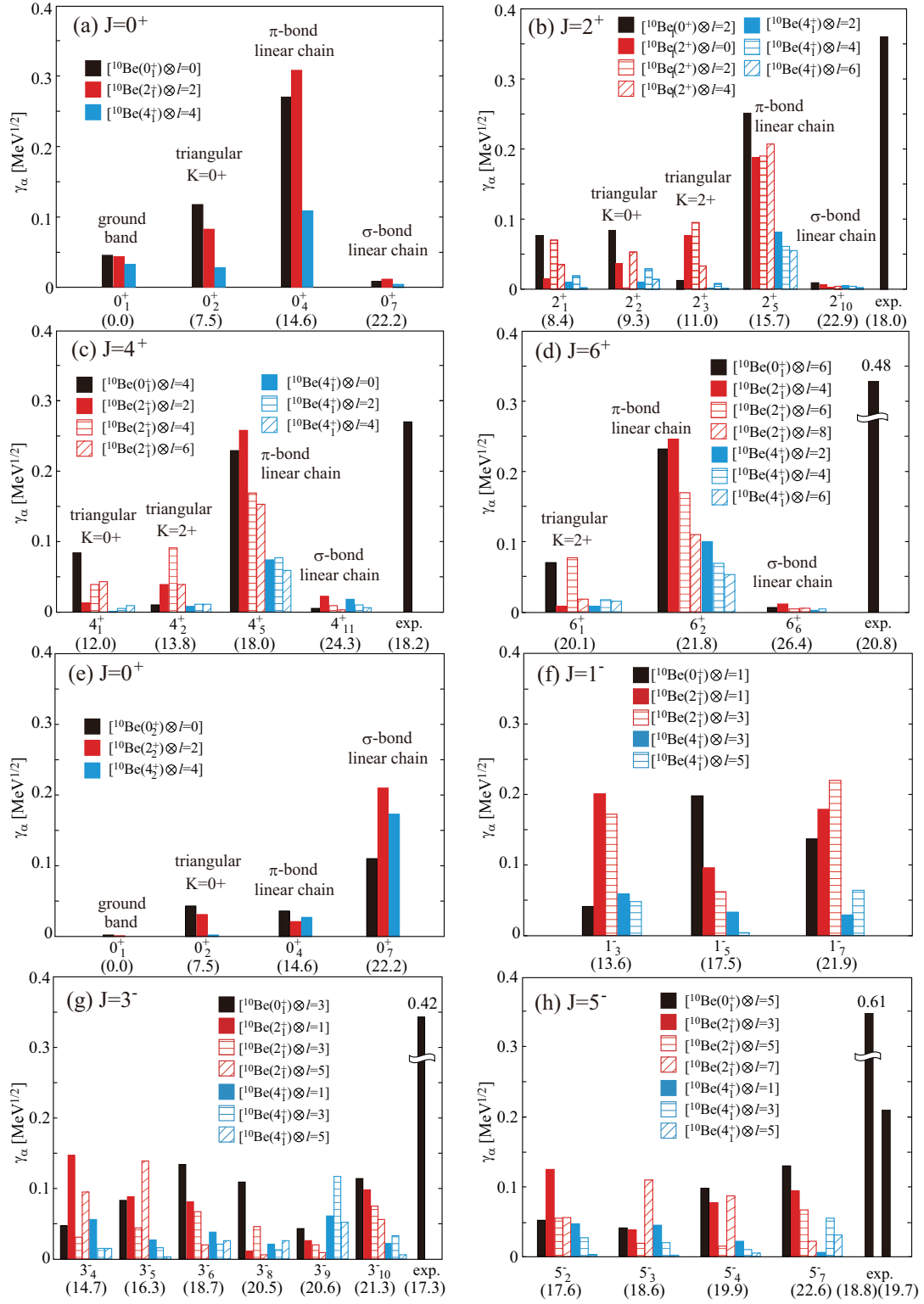


FIG. 8. (color online) The calculated  $\alpha$ -decay reduced widths compared with the observed widths reported in Ref. [29]. Panels (a)-(d) show the decay of the positive-parity states to the ground band of  $^{10}\text{Be}$  ( $\pi$ -bonded  $^{10}\text{Be}$ ). Panel (e) shows the decay of the  $0^+$  states to the excited band of  $^{10}\text{Be}$  ( $\sigma$ -bonded  $^{10}\text{Be}$ ). Panels (f)-(h) show the decay of the negative-parity states to the ground band of  $^{10}\text{Be}$  ( $\pi$ -bonded  $^{10}\text{Be}$ ). Numbers in parenthesis show the excitation energy.

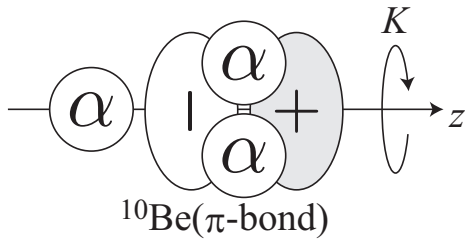


FIG. 9. The schematic figure which explain the relationship between the  $K$  quantum number and the angular momentum of  $^{10}\text{Be}$ .